Nanoscale

Accepted Manuscript

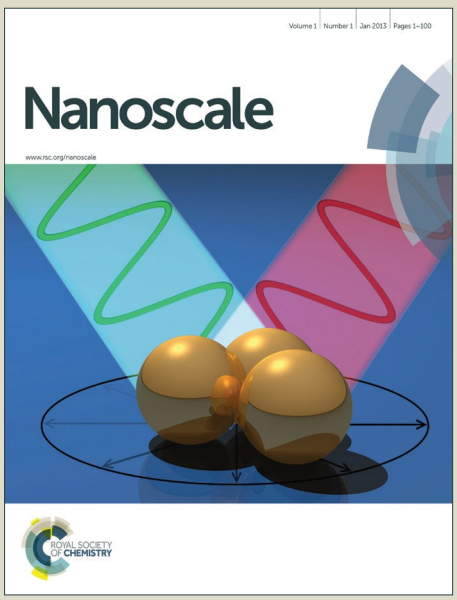

ROYAL SOCIETY OF CHEMISTRY

www.rsc.org/nanoscale

Journal Name

RSCPublishing

ARTICLE

Composition-Property Relationships in Multifunctional Hollow Mesoporous Carbon Nanosystems for PH-Responsive Magnetic Resonance Imaging and On-Demand Drug Releasing

Cite this: DOI: 10.1039/xoxxoooooox

Received ooth January 2012,
Accepted ooth January 2012

DOI: 10.1039/xoxxoooooox

www.rsc.org/

Shengjian Zhang,[a†] Xiaoqing Qian,[c†] Linlin Zhang,[b] Weijun Peng[a*] and Yu Chen[b*]

The construction of intelligent stimuli-responsive nanosystems can substantially improve the sensitivity/resolution/specificity of diagnostic imaging and enhance the therapeutic efficiency of chemotherapy for cancer treatment. This work reports on a generic constructing strategy to achieve the multiple stimuli-responsive theranostic of cancer simply by optimizing the chemical compositions of inorganic nanoplatforms to avoid the tedious and complicate synthetic procedure for traditional organic or organic/inorganic nanosystems. Based on the "breaking up" nature of manganese oxides and specific feature of carbonaceous framework to interact with aromatic drug molecules, manganese oxide nanoparticles were elaborately integrated into hollow mesoporous carbon nanocapsules by a simple *in-situ* framework redox strategy to realize the concurrent pH-sensitive T_1-weighted magnetic resonance imaging (MRI) and pH-/HIFU-responsive on-demand drug releasing. The ultrasensitive disease-triggered MRI performance has been successfully demonstrated by a 52.5-folds increase of longitudinal relaxivity (r_1 = 10.5 $mM^{-1}s^{-1}$) and on nude mice 4T1 xenograft. The pH- and HIFU-triggered doxorubicin releasing and enhanced therapeutic outcome against multidrug resistance of cancer cells were systematically confirmed. Especially, the fabricated inorganic composite nanocapsules were found to be featured with unique biological behaviours, such as antimetastasis effect, extremely low hemolysis against red blood cells and high *in vivo* histocompatibility. This report on the successful construction of pure inorganic nanosystem with multiple stimuli-responsivenesses may pave the new ways for the development of intelligent nanofamilies for cancer therapy.

1. Introduction

The treatment of cancer *via* an intelligent stimuli-responsive manner provides a highly efficient strategy for personalized cancer medicine typically by employing the unique features of tumor microenvironment *(e.g.*, pH, reducing condition, biomarkers) or clinical external irradiations (*e.g.*, light, ultrasound, magnetic field).[1] On-demand drug releasing can directly deliver and release the therapeutic agents into the targeted tumor tissues to avoid the adversely toxic effects to normal organs.[2] Importantly, the tumor microenvironment-triggered diagnostic magnetic resonance imaging (MRI) can substantially improve the imaging resolution, sensitivity and specificity of tumor tissues.[3] Thus, the development of theranostic nanomedicine (concurrent diagnosis and therapy) are expected to be upgraded into such an intelligent manner with concurrent stimuli-responsive diagnostic imaging and on-demand therapeutic drug releasing performance.[4]

Large amounts of organic nanoparticles (NPs) have been chemically constructed for stimuli-responsive drug releasing and diagnostic imaging, typically by breaking the elaborately incorporated responsive organic groups (*e.g.*, reducing-responsive disulfide bond, pH-responsive ester bond) or directly disintegrating the NPs upon inner and/or outer triggering.[1a, 1d] The instability and lack of functionality of traditional organic nanosystems, however, severely restrict their further clinical translations. Organic-inorganic hybrid nanosystems, especially mesoporous silica-based NPs (MSNs) have been extensively explored as the stimuli-responsive drug delivery nanosystem by capping diverse nanovalves onto the surface of well-defined mesopores.[5] However, the tedious and complicate capping process makes them difficult for large-scale fabrications and industrial/clinical translations. In addition, it still remains a big challenge to construct an intelligent nanoporous platform with simultaneous stimuli-responsive diagnostic imaging and anticancer drug-releasing performance based on traditional MSNs. Compared to inert silica composition, inorganic carbon nanofamilies are generally regarded as safe for biomedical purposes, such as the well-

known two-dimensional graphene,[6] one-dimensional carbon nanotubes[7] and zero-dimensional carbon nanodots.[8] Three-dimensional mesoporous carbon NPs (MCNs) are the new member of inorganic carbon family in nanomedicine due to their well-defined nanoporous structures, uniform morphologies and high biocompatibility. Importantly, the unique carbonaceous framework could endow them with the new functions and specific biological effects superior to mostly reported MSNs.[9] However, the fabrication of MCNs, especially MCNs-based intelligent multifunctional composite nanosystems with high dispersity and hydrophilicity is still very challenging, which is currently regarded as one of the biggest obstacles for their extensive biomedical applications.

2. Results and discussion

2.1 Design, synthesis and characterization of MnOx-HMCNs

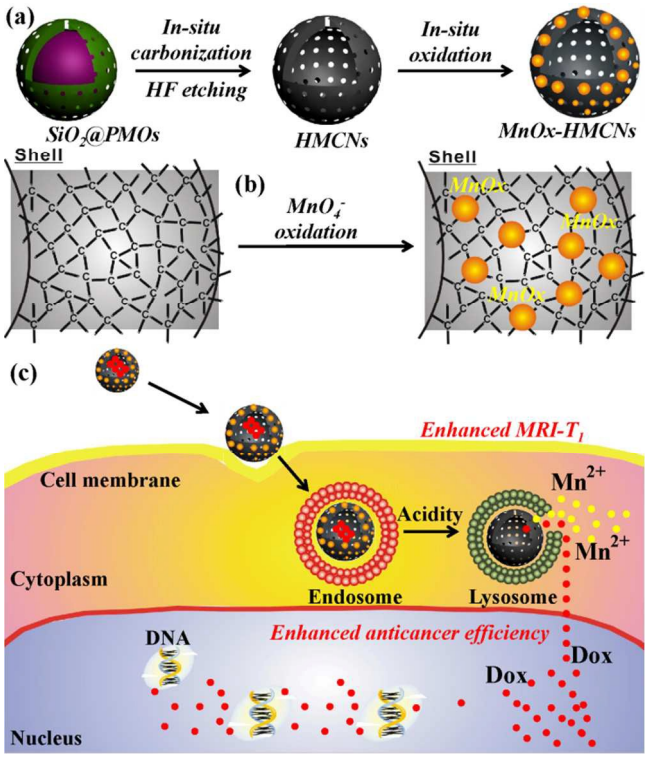

Figure 1. Schematic illustration of (a) synthetic procedure for MnOx-HMCNs, (b) incorporation of MnOx NPs into the framework of HMCNs and (c) cellular uptake and dual pH-responsivenesses of MnOx-HMCNs for T_1-weighted MR imaging and anticancer drug releasing.

Herein, we successfully constructed a highly efficient multiple stimuli-responsive nanoplatform simply by optimizing the chemical compositions of pure inorganic nanosystems, *i.e.*, the elaborate integration of MCNs with biocompatible manganese oxide NPs. Manganese oxide (MnOx)-decorated hollow MCNs (designated as MnOx-HMCNs) can be easily synthesized by a simple, economic and efficient *in-situ* framework redox (is-FR) strategy to realize the concurrent pH-responsive T_1-weighted MR imaging (designated as MRI-T_1) and anticancer drug releasing. As shown in **Figure 1a**, highly dispersed hollow mesoporous carbon nanocapsules (HMCNs) were initially synthesized by directly carbonizing the benzene groups within the framework of periodic mesoporous organosilicas (PMOs) shell of core/shell structured SiO_2@PMOs NPs, followed by HF etching to remove the silica components.[9a, 10] Importantly, the carbonaceous framework of HMCNs is featured with reactively reducing nature.[11] Strongly oxidative potassium permanganate ($KMnO_4$) can *in-situ* react with carbonaceous framework of HMCNs by a redox reaction mechanism, by which MnOx NPs can be *in-situ* generated and incorporated into the framework or onto the surface of HMCNs to form MnOx-HMCNs composite nanocapsules (**Figure 1b**). The paramagnetic Mn centres are initially shielded from aqueous environment because most of them are restricted within the MnOx NPs, resulting in low availability to water and quenched T_1-weighted signal enhancement ("OFF" state). The tumor or intracellular acidic microenvironment can break up the MnOx NPs to release the Mn^{2+} ions after the endocytosis of nanocapsules (**Figure 1c**). The released Mn^{2+} ions in aqueous environment are endowed with maximum availability to interact with water molecules, leading to significantly enhanced MRI-T_1 performance ("ON" state).[12] Such an OFF/ON state transformation can cause 52.5-folds increase of longitudinal relaxivity (r_1), corresponding to the largest relaxivity change yet reported. Importantly, the carbonaceous framework of MnOx-HMCNs can interact with anticancer agents through supramolecular π-π stacking, which has been demonstrated to be highly sensitive to pH variations.[13] Thus, the elaborately designed MnOx-HMCNs can act as the unique nanoplatform with dual stimuli-responsivenesses (imaging and drug releasing) simply by optimizing their chemical compositions.

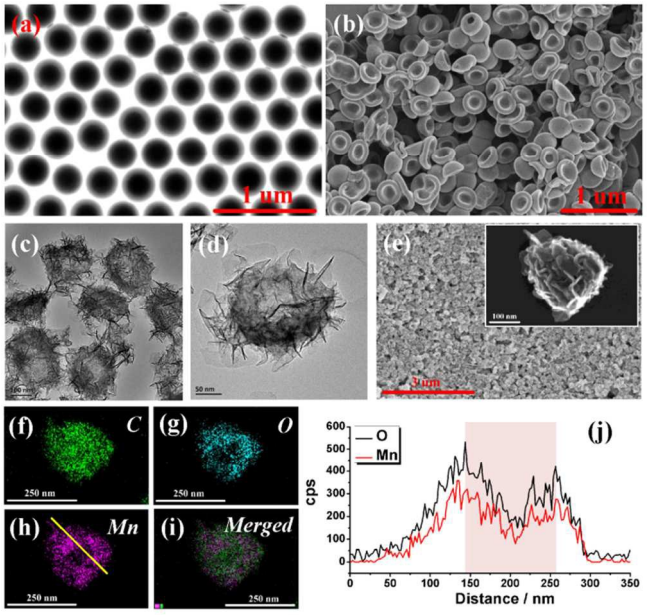

Figure 2. (a) TEM image of SiO_2@SiO_2/C composites; (b) SEM image of RBCs-shaped HMCNs; TEM images of MnOx-HMCNs with low (c) and high (d) magnifications; (e) Low magnification SEM image of MnOx-HMCNs (inset: SEM image with high magnification); (f-i) Surface element mapping of MnOx-HMCNs (f: C, g: O, h: Mn, i: merged image) and (j) corresponding liner element scanning of line in h.

Core/shell structured SiO_2@SiO_2/C NPs can be clearly distinguished in TEM image (**Figure 2a**) by the contrast difference after the carbonization of SiO_2@PMOs. The unique red blood cells (RBCs)-shaped HMCNs after HF etching can be observed in SEM image (**Figure 2b**). After the $KMnO_4$ oxidization, the surface of HMCNs became rough due to the formation of large amounts of MnOx nanosheet-like NPs on the surface (**Figure 2c and d**).

Importantly, the RBC's morphology and high dispersity of HMCNs could be perfectly preserved during the oxidation process, demonstrated by TEM (**Figure 2c and d**) and SEM (**Figure 2e**) characterizations. Surface element mapping gives the direct evidence that Mn element is uniformly distributed within the shell of HMCNs (**Figure 2f-i**), and the line element scanning demonstrates that the hollow nanostructure of HMCNs was well-preserved (**Figure 2j**). The particle size of MnOx-HMCNs is determined to be about 300 nm by dynamic light scattering (DLS, **Figure 3a**). Raman spectra show that the typical D (1340 cm^{-1}) and G (1585 cm^{-1}) peaks of carbon of initial HMCNs became much weaker after the redox process (**Figure 3b**), which could be attributed to the *in-situ* incorporation of MnOx NPs within the framework of HMCNs that can decrease the structural integrity of carbonaceous framework. The newly formed strong peak at Raman shift of around 642 cm^{-1} can be indexed to the Mn-O bond vibration of integrated MnOx NPs.[14] XPS spectrum of Mn2p (**Figure 3c**) shows that three characteristic peaks located at 641 eV, 642 eV and 644 eV could be separated, which are corresponding to two, three and four valence of Mn element, respectively.[15] The characteristic peaks of C1s (**Figure 3d**) located at 285.7 eV is indexed to the surface C-OH or their oxidation forms, and the peak at 287.6 eV is associated with the oxygen in the carbonate ions.[9a] These oxygen-containing bonds can endow MnOx-HMCNs with high hydrophilicity. In addition, the prepared MnOx-HMCNs show the well-defined mesoporous structure with the surface area of 393 m^2/g, pore volume of 0.26 cm^3/g and average pore size of 3.8 nm (**Figure 3e and f**), which provides the channels for transportation and encapsulation of guest molecules. The loading amount of MnOx within HMCNs could be simply controlled by changing the initial concentrations of oxidative MnO_4^- (**Figure 3g-l**).

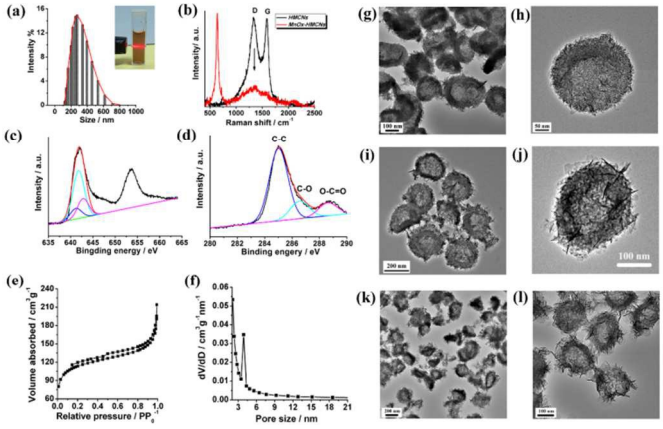

Figure 3. (a) Dynamic light scattering (DLS) of MnOx-HMCNs in aqueous solution (inset: digital photo of MnOx-HMCNs dispersed in water solution to show their high dispersity); (b) Raman spectra of HMCNs and MnOx-HMCNs; (c) Mn2p and (d) C1s X-ray photoelectron spectroscopy (XPS) spectra of MnOx-HMCNs; (e) N_2 adsorption-desorption isotherm and (f) corresponding pore size distribution of MnOx-HMCNs; TEM images with different magnifications of MnOx-HMCNs obtained from different initial $KMnO_4$ concentrations: (g, h): 0.0125 M, (i, j): 0.025 M and (k, l): 0.05 M. TEM images (g-l) show that the only small amounts of MnOx NPs can be observed within HMCNs at the initial low MnO_4^- concentration (0.0125 M, g and h). The loading amounts increase with the elevated MnO_4^- concentrations (i and j, k and l), indicating that the proposed is-FR strategy can simply control the loading amount of MnOx by choosing different initial concentrations of oxidative agents.

2.2 MnOx-HMCNs for stimuli-responsive T_1-weighted MRI

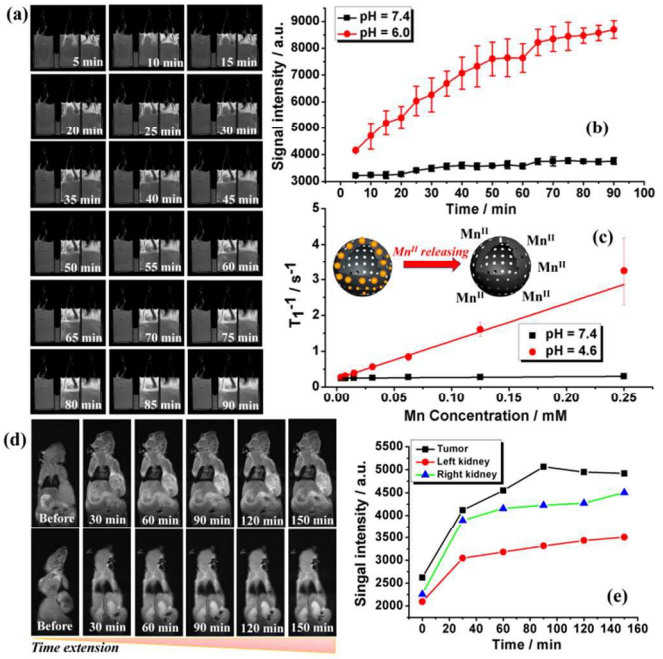

Figure 4. (a) *In-situ* dynamic observation of the *in vitro* pH-responsive contrast-enhanced T_1-weighted MR imaging by impregnating MnOx-HMCNs into the buffer solutions with different pHs (left tube: pH. 7.4, middle tube: pH. 6.0, right tube: pH.4.6) and (b) corresponding signal intensity variations with the extension of impregnation time; (c) T_1^{-1} versus Mn concentrations of MnOx-HMCNs after the treatment in pH. 7.4 and pH. 4.6 buffer solutions; (d) *In vivo* MR imaging of tumor (upper image) and kidney (down image) before and after intravenous administration of MnOx-HMCNs for different durations and (e) the corresponding quantitative signal intensity changes.

Manganese oxides NPs are featured with unique "breaking up" feature, which can release the Mn^{2+} ions in acidic environment.[16] The gradually generated paramagnetic Mn^{2+} ions in acidic condition possess the maximum chances to interact with water molecules, leading to the significantly enhanced MRI-T_1 performance.[12a, 16-17] This unique disintegration nature of MnOx NPs is very beneficial for tumor diagnostic imaging due to the acidic microenvironment of tumor tissues caused by the high level of lactic acid induced by up-regulated glycolytic metabolism, which has been extensively explored as the biomarker of tumorigenesis or the triggers for on-demand drug releasing.[1b, 12a] In addition, the disintegration of MnOx NPs can facilitate their excretion out of the body. To directly observe the concurrent dynamic breaking up of MnOx NPs, leakage of Mn^{2+} ions and gradual positive-signal enhancement of MRI-T_1, MnOx-HMCNs were sealed within a dialysis bag, which was then immerged into the buffer solution with different pHs (pH. 7.4, 6.0 and 4.6). The released Mn^{2+} can penetrate through the dialysis bag but the MnOx-HMCNs are too big to pass through it. As shown in **Figure 4a**, a significant MRI-T_1 signal enhancement can be observed around the dialysis bag of acidic buffer solution (pH. 6.0 and 4.6) within a short period (5 min), and this unique signal enhancement gradually extends into the whole buffer solution in the prolonged duration. Comparatively, the MnOx-HMCNs immerged within neutral buffer solution gives no obvious signal enhancement. The quantitative MRI-T_1 signal variations (**Figure 4b**) show that the

MRI-T_1 signal intensity in pH. 6.0 buffer solution is 2.3 times higher than the one of neutral buffer solution after 90 min-immersion. This *in-situ* and real-time dynamic MR imaging of MnOx-HMCNs gives the strong evidence that the integrated MnOx NPs within HMCNs are ultrasensitive to the acidic condition to trigger the release of Mn^{2+} ions and enhance the MRI-T_1 performance accordingly.

The longitudinal relaxivity r_1 of MnOx-HMCNs in neutral buffer solution was calculated to be only 0.20 $mM^{-1}s^{-1}$ (**Figure 4c**) due to the shielding effect of paramagnetic centres within the NPs, which is similar to the reported relaxivity of 15 nm MnO NPs (0.20 $mM^{-1}s^{-1}$).[18] The relaxivity gives a substantial increase to 10.5 $mM^{-1}s^{-1}$ after the treatment of MnOx-HMCNs in pH. 4.6 buffer solution, which is the highest value for reported MnOx NPs-based contrast agents (CAs) of MRI-T_1, and is much higher than reported 7 nm MnO NPs (0.37 $mM^{-1}s^{-1}$),[18] SiO_2-coated manganese oxide NPs (0.47 $mM^{-1}s^{-1}$),[19] human serum albumin-coated MnO NPs (1.97 $mM^{-1}s^{-1}$),[20] mesoporous silica-coated hollow manganese oxide NPs (0.99 $mM^{-1}s^{-1}$)[12b] and manganese oxide NPs-dispersed within mesopores (2.28 $mM^{-1}s^{-1}$).[21] The unique composition of manganese oxides and their spcific acidity-induced "breaking up" feature contribute to such a 52.5-folds increase of longitudinal relaxivity (r_1).

To demonstrate the *in vivo* ultrasensitive contrast-enhanced MRI-T_1 performance, MnOx-HMCNs saline solution was intravenously administrated into nude mice bearing 4T1 breast cancer xenograft. It was found that the tumor margin became much brighter after 30 min-administration of MnOx-HMCNs saline solution (**Figure 4d**), which was due to the passive-targeted accumulation of MnOx-HMCNs within tumor tissues by enhanced permeability and retention (EPR) effect. Importantly, the significantly enhanced MRI-T_1 signal could be observed within the whole tumor tissues after the 90 min post injection. The mild acidic microenvironment of tumor tissues caused the breaking up of MnOx NPs within HMCNs to gradually release the highly MRI-positive Mn^{2+} ions. The generated ultrasmall Mn^{2+} ions could easily penetrate into the tumor tissues to highlight the whole tumor by MRI-T_1. In addition, the Mn^{2+} ions were so small that they could be easily excreted from the tumor tissues, causing the slight decrease of MRI-T_1 signals along with the prolonged time (120 min and 150 min). The MRI-T_1 signal variation of tumor was quantitatively shown in **Figure 4e**. The leakage of Mn^{2+} ions was also directly demonstrated by the MRI-T_1 signal enhancement of kidney (down image of **Figure 4d** and **Figure 4e**). It was shown that the MRI-T_1 signal intensity of kidney increased gradually with the extension of post-injection time, indicating that the CAs entered the kidney. It has been well-demonstrated the ultrasmall particle sizes of less than 5.5 nm are able to penetrate into the kidney.[22] Obviously, the whole particle size of MnOx-HMCNs is beyond this size limitation. Therefore, it was only caused by the generated Mn^{2+} ions with ultrasmall size those could enter the kidney to cause such a positive signal enhancement, which also gave an indirect but convincing evidence of the disintegration of MnOx-HMCNs to release Mn^{2+} ions. It was further demonstrated that the MnOx-HMCNs could also act as the *in vitro* and *in vivo* CAs for ultrasound (US) imaging due to their unique hollow core/shell structure, indicating that they could function as the dual-modality CAs for MR/US imaging (**Figure S1 and S2**).

2.3 MnOx-HMCNs for stimuli-responsive drug releasing

The carbonaceous composition not only can react with MnO_4^- to *in-situ* integrate with functional MnOx NPs, it can also interact with aromatic drug molecules through supramolecular π-π stacking (**Figure 5a**).[13, 23] Such a unique interaction is highly stimuli-responsive, which could be interfered by either intrinsic mild acidic tumor microenvironment or outer artificially introduced triggers, such as ultrasound. Thus, MnOx-HMCNs composite NPs can not only respond to pH variations for MRI-T_1, but also can release the loaded cargos *via* an intelligent on-demand manner. A typical aromatic anticancer drug, doxorubicin (Dox), was loaded into MnOx-HMCNs with the high loading amount of 375 mg/g, which was attributed to the large hollow interiors, well-defined mesopores of the composite nanocapsules and special interactions between carbonaceous framework and Dox molecules.[24]

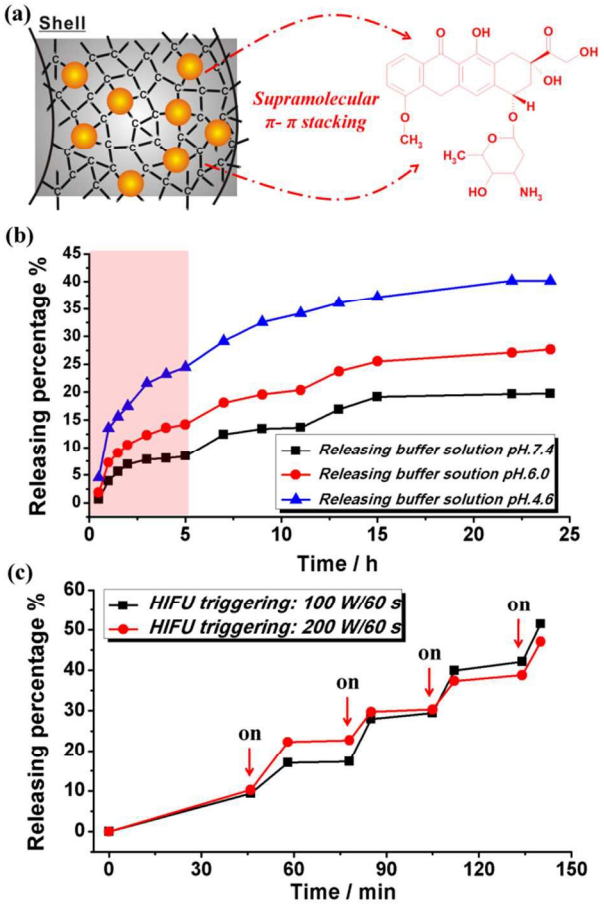

Figure 5. (a) Schematic illustration of supramolecular π-π stacking between the carbonaceous framework and Dox molecules; (b) Dox-releasing percentage from Dox-loaded MnOx-HMCNs under different pHs (pH.7.4, 6.0 and 4.6); (c) HIFU-triggered Dox-releasing percentage under different irradiation parameters (100 W/60 s and 200 W/60s).

The *in vitro* on-demand drug-releasing behaviours of Dox-loaded MnOx-HMCNs were firstly investigated within buffer mediums with different pHs (pH. 7.4, 6.0 and 4.6). The acidic releasing medium was used to mimic the intrinsic tumor acidic microenvironment. As shown in **Figure 5b**, the Dox-loaded MnOx-HMCNs exhibit the slow releasing profile at neutral buffer solution, but the releasing rate accelerates significantly in mild acidic buffer mediums. The 5h-releasing amount in neutral condition was only 8.4%. However, 14.2% and 24.5% releasing percentages could be achieved within 5 h in pH. 6.0 and pH. 4.6 buffer solutions, respectively. Such a pH-responsive drug releasing behaviour was based on the unique supramolecular π-π stacking between the carbonaceous framework and aromatic Dox molecules, which could

be interfered and broken in the mild acidic environment. Importantly, such a special non-covalent π-π stacking could also be broken by external triggering. One of the most important external triggers is ultrasound due to its high tissue penetration capability and easily handing nature.[25] **Figure 5c** shows that the introduced high intensity focused ultrasound (HIFU) could significantly accelerate the releasing rate of Dox from MnOx-HMCNs, which exhibits a unique pulse-type Dox-releasing patterns corresponding to the on/off of the HIFU irradiations. The high mechanical effect of focused ultrasound can induce the fast separation of Dox molecules from the carriers, which is regarded as the main cause for focused ultrasound-based on-demand drug-releasing patterns.

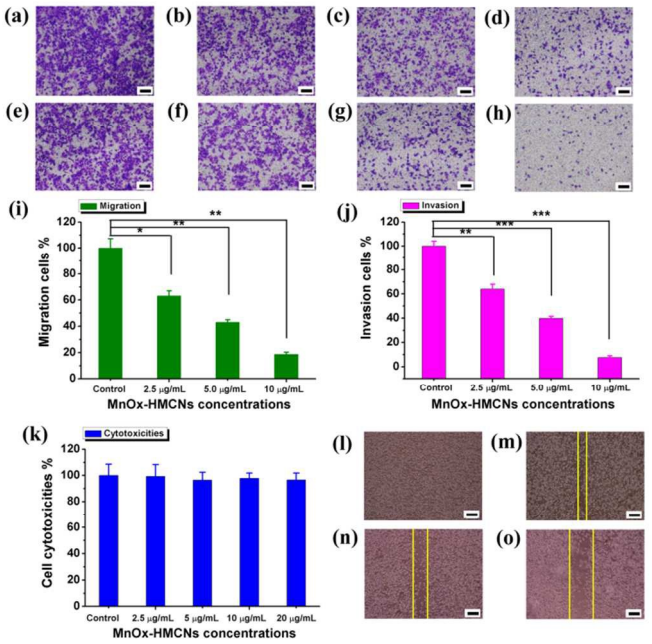

Figure 6. Optical microscopic images of migrated (a-d) and invasive (e-h) MDA-MB-231 cells after the co-incubation without (a, e) and with MnOx-HMCNs at different concentrations (b, f: 2.5 μg/mL, c, g: 5 μg/mL and d, h:10 μg/mL); Quantitative percentages of migrated cells (i) and invasive cells (j); (k) Cell viabilities of MDA-MB-231 cells after the co-incubation with MnOx-HMCNs for 24 h at different concentrations; Wound-healing assay of MDA-MB-231 cells after the co-incubation without (l) and with MnOx-HMCNs at different concentrations (m: 2.5 μg/mL, n: 5 μg/mL and o: 10 μg/mL). Scale bars of a-h and l-o: 200 μm.

It was anticipated that the unique composition and nanostructure of MnOx-HMCNs might cause some unique biological effects on the migrations and invasion of metastasis cancer cells. As shown in **Figure 6**, the migration capability of metastatic MDA-MB-231 breast cancer cells could be significantly inhibited after the co-incubation with MnOx-HMCNs composite NPs (**Figure 6a-d**). Compared to control cells, the migrated cell percentage was only 18.6% at the concentration of 10 μg/mL (**Figure 6i**). To further mimic the practical metastatic environment, the invasive capability of MDA-MB-231 cancer cells was investigated by determining their invasion process across the transwell chamber with a layer of coated matrigel. It was found that the invasive ability of metastatic MDA-MB-231 cells could also be significantly inhibited (**Figure 6e-h**), causing only 7.6% invasive cancer cells compared to the control metastatic cells (**Figure 6j**). The cell cytotoxicities of MnOx-HMCNs show that MnOx-HMCNs exhibit no obvious cytotoxicities against MDA-MB-231 cells (**Figure 6k**), indicating that the significant inhibition feature of MnOx-HMCNs was not caused by the cytotoxicity effects. The wound-healing assay also indicates that the migration capability of cancer cells was significantly inhibited to delay the healing of the artificially generated wounded areas (**Figure 6l-o and S3**), which gives the indirect evidence that the introduction of MnOx-HMCNs could inhibit the metastasis behaviour of cancer cells. It was believed that the uptake of MnOx-HMCNs could significantly decrease the expression of metastasis-related proteins (*e.g.*, MMP, Snail, uPA, et al) to further inhibit the metastasis of cancer cells.[9a, 26]

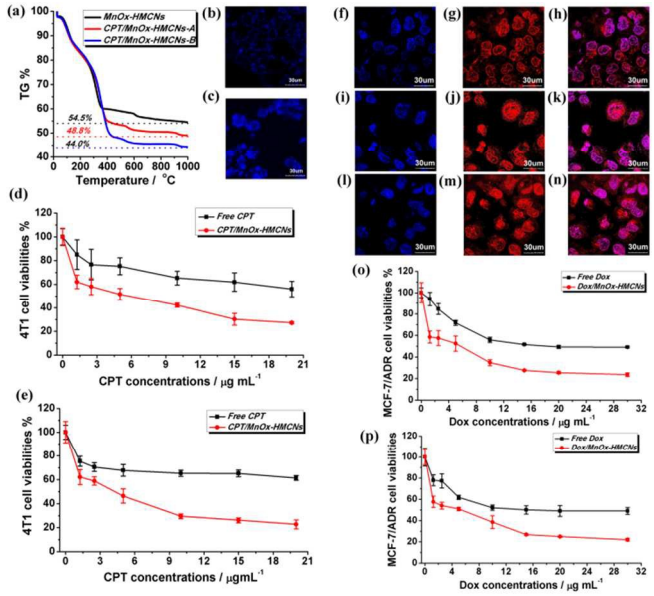

Figure 7. (a) TG curves of MnOx-HMCNs and CPT-loaded MnOx-HMCNs (A and B represent that the initial CPT concentrations for drug loading were 2 mg/mL and 4 mg/mL, respectively); CLSM images of 4T1 cells after the co-incubation with CPT-loaded MnOx-HMCNs for (b) 4 h and (c) 8 h; Cell viabilities of 4T1 cells after the treatment with free CPT and CPT/MnOx-HMCNs for (d) 12 h and (e) 24 h; CLSM images (f, i and l: blue DAPI fluoresce, g, j and m: red Dox fluorescence, h, k and n: merged image of blue and red fluorescence) of MCF-7/ADR cells after the incubation with Dox-loaded MnOx-HMCNs for (f-h) 4 h, (i-k) 8 h and (l-n) 12 h; Cell viabilities of MCF-7/ADR cells after co-incubation with free Dox and Dox/MnOx-HMCNs for (o) 24 h and (p) 48 h.

The carbonaceous composition and large hollow interiors of MnOx-HMCNs are expected to show high performance for the encapsulation and transport of hydrophobic anticancer drugs, which is of great significance in medicine because more than 40% of chemotherapeutic agents selected by combinatorial screening program are hydrophobic.[27] The hydrophobic nature of these agents shows the ultralow bioavailability and therapeutic efficiency. To validate this idea, a typical anticancer drug, camptothecin (CPT), was chosen for the systematic evaluations. From thermo-gravimetric curves (**Figure 7a**), it was found that the MnOx-loading amount within MnOx-HMCNs could reach 35.3%, and the drug loss was calculated to be as high as 5.7% and 10% with the initial CPT-loading concentrations of 2 mg/mL and 4 mg/mL, respectively. This drug-loading amount is significantly higher than traditional MSNs (typically < 1%),[28] which could be attributed to the possible drug molecule-carbonaceous framework interactions and hollow interiors as the large reservoirs for drugs. The intracellular CPT delivery

mediated by MnOx-HMCNs was directly observed by confocal laser scanning microscopy observations (CLSM, **Figure 7b and c**). It was found that large amounts of blue fluorescent dots representing CPT-loaded MnOx-HMCNs were present within the cytoplasm of 4T1 breast cancer cells (**Figure 7b**), indicating that CPT/MnOx-HMCNs could be endocytosized into cancer cells. When the incubation time was extended to 8 h, a significant strong blue fluorescence could be observed within the whole cells (**Figure 7c**), indicating the gradual release of CPT from MnOx-HMCNs within the cells. A typical MTT protocol was adopted to evaluate the therapeutic efficiency of CPT-loaded MnOx-HMCNs against cancer cells. The results show that CPT-loaded MnOx-HMCNs exhibit significantly enhanced cytotoxicities than free CPT molecules. The inhibition rates of CPT/MnOx-HMCNs could reach 72.7% and 77.2% after 12 h (**Figure 7d**) and 24 h (**Figure 7e**) co-incubation at the equivalent CPT concentration of 20 μg/mL, respectively. Comparatively, the free CPT could only induce the inhibition rates of 44.0% (12 h) and 36.8% (24 h) at the same co-incubation conditions. Such an enhanced therapeutic efficiency is based on the enhanced intracellular amounts of CPT delivered by MnOx-HMCNs and corresponding increased bioavailability of hydrophobic drugs.

The intracellular delivery of hydrophilic anticancer drugs was demonstrated by choosing Dox as the therapeutic agent against Dox-resistant MCF-7/ADR breast cancer cells. It was found that large amounts of Dox molecules could be delivered into MCF-7/ADR cancer cells (**Figure 7f-n and S4**), demonstrated by the presence of strong red fluorescence representing Dox. The intracellular fluorescence intensity increases with the extension of co-incubation time (4 h, 8 h and 12 h). Importantly, MnOx-HMCNs-medicated Dox delivery could circumvent the multidrug resistance (MDR) of Dox-resistant MCF-7/ADR cancer cells. The inhibition rates using Dox/MnOx-HMCNs are 76.4% and 78.0% at the Dox concentration of 30 μg/mL after 24 h (**Figure 7o**) and 48 h (**Figure 7p**) co-incubation, respectively. The presence of P-glycoproteins on the surface of cell membrane of MCF-7/ADR cells can pump the Dox molecules out of the cells, causing only 50.9% (24 h) and 51% (48 h) inhibition rates at the same co-incubation conditions. It was reported that the size of P-glycoproteins entrance channel was no more than 3 nm,[29] thus the MnOx-HMCNs with relative large particle sizes could not be effluxed from the cells, causing the significantly enhanced anticancer efficiencies.[30]

2.4 Biocompatiblity evaluations of MnOx-HMCNs

The unique carbonaceous and manganese oxide-based compositions endow MnOx-HMCNs with superior biocompatibilities for biomedical applications. Compared with traditional mesoporous silica nanoparticles (MSNs), the carbonaceous NPs lack the typical silanols (Si-OH) present on the particles' surface, which are generally regarded as the dominant factors causing the severe hemolysis of RBCs. Thus, it was expected that MnOx-HMCNs composite NPs exhibited low hemolytic effects against RBCs. To validate this idea, MnOx-HMCNs were incubated with RBCs to evaluate their hemolytic effects by a standard process.[31] As shown in **Figure 8**, there are no obvious hemolytic effects after co-incubating either HMCNs or MnOx-HMCNs with RBCs, demonstrated by both the qualitative visual inspection (**Figure 8a and b**) and quantitative UV-vis calculations (**Figure 8c**). At the NPs' concentration of as high as 1000 μg/mL, the hemolytic percentages of HMCNs and MnOx-HMCNs are only 2.8±0.28% and 1.2±0.25%, respectively. It was reported that the hemolytic effect of MSNs at the concentration of 1000 μg/mL was as high as more than 90%,[32] thus the surface modifications such as PEGylation[31a] or incorporation of functional organic groups (*e.g.*, ethenylene,[32] benzene[10]) were generally required to reduce their hemolytic effect. In MnOx-HMCNs inorganic nanosystems, their unique chemical compositions can directly show the negligible hemolytic effects, demonstrating their high hematological biocompatibility.

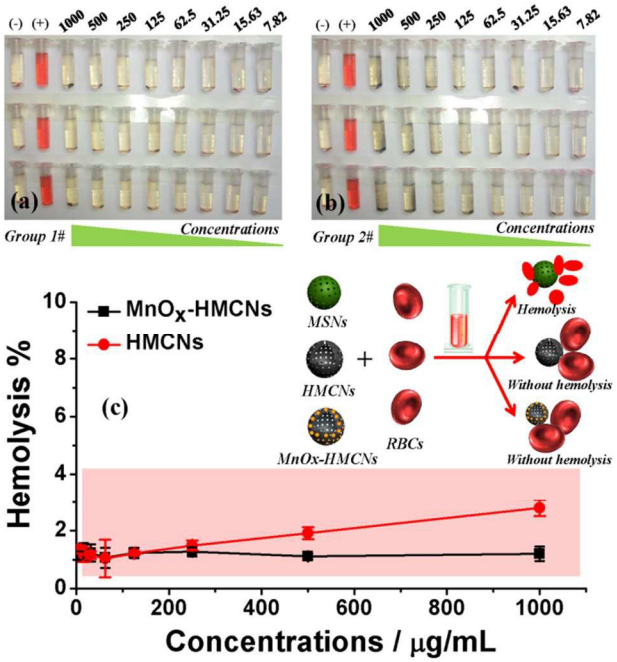

Figure 8. Digital images of RBCs after co-incubation with HMCNs (a, Group 1, n = 3) and MnOx-HMCNs (b, Group 2, n = 3) for 2 h (PBS was used as the negative control while water was employed as the positive control); (c) Hemolytic percentages of RBCs after the incubation with HMCNs and MnOx-HMCNs (inset: schematic illustration of hemolysis evaluation of MSNs, HMCNs and MnOx-HMCNs against RBCs and their hemolytic effects).

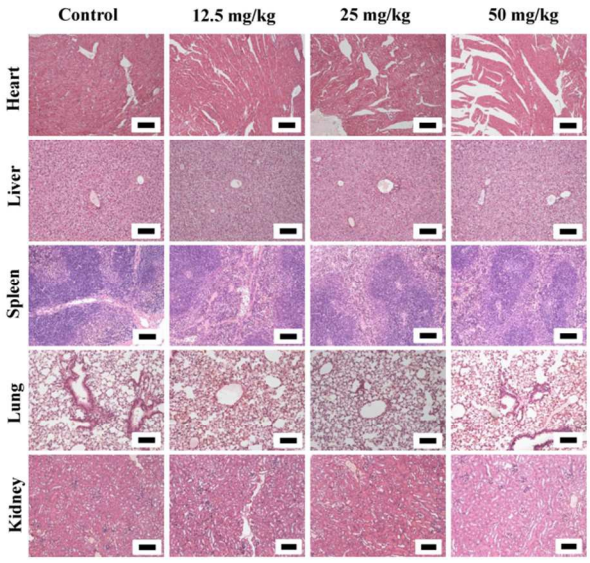

Figure 9. Optical microscopic images of main organs (heart, liver, spleen, lung and kidney) of MnOx-HMCNs-treated healthy nude mice after histological hexatoxylin eosin (HE) staining. The mice were intravenously received MnOx-HMCNs saline solution with different doses (12.5, 25 and 50 mg/kg), and feed for 30 days. Scale bars of all images: 100 μm.

To further demonstrate *in vivo* biocompatibility, MnOx-HMCNs saline solution was intravenously administrated into healthy nude mice with different doses (12.5, 25 and 50 mg/kg). No abnormal behaviours or death of mice were observed during the 30 days observations. After the histopathological examinations of heart, liver, spleen, lung and kidney by the typical hexatoxylin eosin (HE) staining (**Figure S5 and 9**), no obvious pathological toxicities were observed compared to the control mice, even at the doses of as high as 50 mg/kg. Both hemolytic evaluation and histopathological examination show the high bio-safety of MnOx-HMCNs, indicating their potential clinical translation prospects.

It is considered that the release of Mn^{2+} can cause the potential toxicity to cells. It is well-known that the MRI performance is influenced by the administration dose of CAs. The disintegration of MnOx to release Mn^{2+} can significantly enhance the imaging performance of CAs, which means that much lower doses of CAs can be used to achieve the desirable MRI performance, thus the toxicity can be significantly mitigated. In addition, manganese ion is also an essential and daily required metal to human beings because the manganese is the necessary element for physiological metabolism and the biological systems can efficiently control its homeostasis. The release of ultrasmall Mn^{2+} can be quickly excreted out of the body *via* the kidney. Based on these considerations, it is expected that MnOx-HMCNs can act as the biocompatible CAs for T_1-weighted MR imaging.

3. Conclusions

In summary, a generalizable concept has been presented to construct highly efficient multiple stimuli-responsive nanosystems simply by optimizing the chemical composition of inorganic nanosystems. HMCNs and MnOx NPs were elaborately integrated together by a simple and direct chemical redox reaction between reducing carbonaceous framework and oxidizing MnO_4^-. The fabricated MnOx-HMCNs exhibited the unique ultrasensitive pH-responsive MRI-T_1 performance where the relaxivity gives a 52.5-folds increase after the change of neutral solution to mild acidic one. The special supramolecular π-π stacking between carbonaceous framework of MnOx-HMCNs and aromatic drug molecules was further adopted to construct intelligent pH-/ultrasound-sensitive drug-releasing nanoplatforms, which exhibits the unique antimetastasis effect and the high performance of reversing the MDR of cancer cells. The optimized chemical composition of MnOx-HMCNs with disease-triggered features and specific improved biocompatibility (*e.g.*, negligible hemolysis and high histocompatibility) show the great application potentials for clinical personalized medicine, and their construction strategy paves a new way for the development of intelligent nanosystems for cancer therapy.

4. Experimental section

Materials. 1.4-bis(triethoxysilyl)benzene (BTEB) and cetyltrimethyl ammonium bromide (C_{16}TAB) were bought from Sigma-Aldrich. Hydrofluoric acid (HF, 40%), tetraethyl orthosilicate (TEOS), dimethyl sulfoxide (DMSO), potassium permanganate ($KMnO_4$) and ethanol were purchased from Sinopharm Chemical Reagent Co. Chemotherapeutic agent doxorubicin (Dox) was obtained from Beijing HuaFeng United Technology Co., Ltd and camptothecin (CPT) was purchased from Knowshine (Shanghai) Pharmachemicals Inc. Phosphate buffer solution (PBS) with the pH.7.4 was got from Shanghai Ruicheng Bio-Tech Co., Ltd. Citrate acid-sodium citrate buffer solutions with the pHs of 6.0 and 4.6 were laboratory-formulated (0.1 M). Human red blood cells were kindly provided by Shanghai Blood Center. For *in vitro* cell experiment, trypsin-EDTA and fetal bovine serum (FBS) were bought from Gibco-BRL (Burlington, Canada). Dulbecco's Modified Eagle's Medium (DMEM) were purchased from Invitrogen (Oregon, USA), and the matrigel was got from Biosciences (San Jose, USA). All chemicals were used as-received without the purification procedure. Deionized water was adopted for the whole synthetic process.

Synthesis of MnOx-HMCNs. The synthesis of MnOx-HMCNs consists of two steps: the fabrication of HMCNs and further MnOx integration. The synthesis of HMCNs was according to our previous report.[9-10] Typically, TEOS (6 mL) was adding into a mixture containing deionized water (10 mL), ethanol (74 mL) and ammonia solution (3.14 mL), which was stirred at 30°C for 1 h. The resultant as-formed SiO_2 solution was dropped into another as-prepared mixture with deionized water (100 mL), C_{16}TAB ethanol/water solution (30 mL, V(water):V(ethanol) = 2:1, 0.11 M) and ammonia solution (3 mL). After the stirring at 30°C for 0.5 h, BTEB (3 mL) was quickly added into above solution followed by another reaction process at 30°C for 6 h. The as-synthesized SiO_2@PMOs were collected by centrifugation and washed with ethanol and water for several times. Finally, SiO_2@PMOs were freeze-dried and further carbonized at 900°C for 4 h under the protection of N_2. HMCNs were formed by HF etching (10 wt%, 24 h) to remove the SiO_2 component. For MnOx-integration process, the as-synthesized HMCNs were firstly oxidized by concentrated HNO_3 and H_2SO_4 mixture (V_{HNO3}:V_{H2SO4} = 1:2) to endow them with high hydrophilicity. Then, the as-oxidized HMCNs were dispersed into fresh $KMnO_4$ aqueous solution with elevated concentrations (0.0125, 0.025 and 0.05 M) by ultrasound treatment. The mixture was stirred at room temperature in the dark for 4 h, followed by centrifugation to collect the products. The products were further washed with plenty of water, and finally dispersed into water solution.

***In vitro* and *in vivo* pH-responsive magnetic resonance imaging.**[4] The Mn concentration of concentrated MnOx-HMCNs aqueous solution was firstly determined by inductively coupled plasma atomic emission spectrometry (ICP-AES). Before MRI scanning, MnOx-HMCNs were firstly treated in the buffer solution at different pHs (pH. 7.4, 6.0 and 4.6) for 2 h at 37°C, which was shaken at the speed of 100 rpm. Then, the MnOx-HMCNs were diluted with corresponding buffer solution containing xanthan gum (1 mg/mL). The Eppendorf tubes (1.5 mL volume) containing MnOx-HMCNs with different concentrations (1.0 mL) were scanning by a clinical MRI apparatus (GE Signa 3.0 T). The T_1-weighted Fast-recovery spin-echo (FR-FSE) sequence is TR = 1000, 2000, 3000 and 4000, Slice = 3 mm, Space = 0.5 mm, Fov = 20, Phase fov = 0.8, Freq × Phase = 384 × 256, Nex = 2, ETL = 2.

For *in-situ* and real-time observation of the dynamic contrast-enhanced MRI imaging procedure, MnOx-HMCNs aqueous solution was initially encapsulated into a dialysis bag (cutoff molecular weight: 5000 Da), which was then impregnated into the buffer solutions with different pHs. The T_1-weighted MRI images were acquired every five minutes.

The 4T1 orthotopic mammary tumor xenograft was established for the *in vivo* diagnostic MR imaging. 4T1 cells suspended within 50 μL sterile PBS was subcutaneously injected into the mammary fat pad of female nude mouse. All the animal procedures were performed under the guideline approved by the Institutional Animal Care and Use Committee (IACUC) of the Shanghai Institute of Materia Medica, Chinese Academy of Sciences (CAS). After two weeks, the mice were administrated by MnOx-HMCNs saline solution with the Mn dose of 2.5 mg/kg. T_1-weighed MR images

were acquired before and after the intravenous administration of MnOx-HMCNs saline solution at given time intervals.

***In vitro* and *in vivo* ultrasound imaging using MnOx-HMCNs as the contrast-enhanced ultrasound contrast agents.** MnOx-HMCNs aqueous solution with different concentrations (0, 2.5, 5 and 10 mg/mL) was put into Eppendorf tube, which was then immersed into the water tank. The ultrasound imaging was carried out by attaching the ultrasound probes onto the surface of Eppendorf tubes under the harmonic mode with different mechanical indexes (MI = 0.5, 0.6 and 0.7). The average gray vales of ultrasound images were analyzed with SONOMATH-DICOM software.

In vivo ultrasound imaging was carried out on nude mice bearing 4T1 breast cancer xenograft. Typically, the mice were anesthetized followed by *in-situ* intratumorly administration with MnOx-HMCNs saline solution (100 μL, 5 mg/mL). The ultrasound images were acquired before and after the administration of contrast agents under the harmonic imaging mode. Saline solution was used as the control with the same experimental procedure as the MnOx-HMCNs saline solution. The average gray values of tumor tissues were analyzed by SONOMATH-DICOM software.

Encapsulation of CPT and Dox into MnOx-HMCNs and pH-/HIFU-responsive Dox-releasing from MnOx-HMCNs. For CPT loading, MnOx-HMCNs (10 mg) was dispersed into CPT DMSO solution with different concentrations (5 mL, 2 mg/mL and 4 mg/mL), followed by the stirring at room temperature for 24 h. The CPT-loaded MnOx-HMCNs was collected by centrifugation and dried under vacuum at room temperature. The CPT-loading amount on MnOx-HMCNS was determined by TG test. For Dox loading, MnOx-HMCNs (10 mg) were added into Dox PBS solution (20 mL, 0.3 mg/mL). After the stirring at room temperature in the dark for 24 h, the Dox-loaded MnOx-HMCNs were obtained by centrifugation and freeze-dried. The Dox-loading amount was calculated by testing the initial Dox PBS solution and supernatant after centrifugation by UV-vis at the wavelength of 480 nm.

For pH-responsive Dox releasing, Dox/MnOx-HMCNs (3 mg) were encapsulated into a dialysis bag (cutoff molecular weight: 5000 Da), which was then encapsulated into the releasing buffer solution at different pHs (pH. 7.4, 6.0 and 4.6; 30 mL). Then, it was transferred into a shaking table at 37^{o}C with a shaking speed of 100 rpm. At given time, partial releasing medium was taken out for UV-vis test, which was then put back into the initial releasing medium for continuous observation of the releasing behaviour.

For HIFU-trigger Dox releasing, Dox/MnOx-HMCNs (5 mg) were initially dispersed into PBS solution (1 mL), following by putting them into the dialysis bag (cutoff molecular weight: 5000). The dialysis bag was then put into a baker containing PBS with the volume of 50 mL. The focal point of HIFU was facing the dialysis bag containing Dox/MnOx-HMCNs. HIFU was introduced to act on the Dox/MnOx-HMCNs, by which the loaded Dox could be released from the carrier. The pulse wave-HIFU with the irradiation parameters of 100 W/60 s and 200 W/60 s were adopted. Partial releasing medium (5 mL) was taken out for UV-vis test at given time, followed by adding free releasing medium (5 mL). For pulse wave-HIFU triggering, other important parameters are focal length: 50 mm, continuous emission of 2 s/interval 1 s, repeated for 30 times, then interval 20 min.

***In vitro* antimetastasis evaluations.** The biological effects of MnOx-HMCNs on the metastasis of cancer cells were evaluated against the typical metastatic MDA-MB-231 breast cancer cells. Firstly, MDA-MB-231 cells were co-incubated with MnOx-HMCNs at different concentrations for 24 h, which were further digested by trypsin, harvested and suspended in a serum-free cell-culture medium. The obtained cell suspensions (0.1 mL, 2×10^4 cells) were put into the upper transwell chambers (Corning, USA), followed by adding the complete media (0.5 mL, 10% FBS) into the lower chambers as the chemo-attractants. Cells on the surface of upper transwells were removed by cotton swabs after the 18 h-incubation. The migrated cells through the transwell membranes were present on the lower surface of transwells, which were further fixed by 90% ethanol and stained with crystal violet to facilitate the observation by optical microscope. The quantitative results were acquired by counting the cell numbers in six separate 200× fields. For invasion assay, the transwell chambers pre-coated with Matrigel (BDBioscience) were employed and 1×10^5 cells/well was used. Other evaluation procedure was the same as the migration assay. For wound-healing evaluation, MDA-MB-231 cells were initially treated with MnOx-HMCNs at 37°C for 24 h, followed by generating scratch wounds using a 10 μL pipette tip. Cells were washed with PBS for three times. After the further co-incubation for 24 h, the cell images were acquired by an optical microscope.

Confocal laser scanning microscopic (CLSM) imaging of 4T1 and MCF-7/ADR cancer cells. 4T1 and MCF-7/ADR cancer cells were firstly seeded onto a CLSM-specific culture dish with the cell density of around 50%-60%. After the co-incubation with either CPT/MnOx-HMCNs (CPT concentration: 10 μg/mL) or Dox/MnOx-HMCNs (Dox concentration: 10 μg/mL) for different durations, the cells were washed with PBS for three times. The nuclei of MCF-7/ADR cells were staining with DAPI according to the procedure of kit instructions (Cell Apoptosis DAPI Detection Kit, KeyGEM). Finally, the cells were observed in a confocal laser scanning microscope (FV1000, Olympus).

The evaluation of the therapeutic efficiencies of CPT/MnOx-HMCNs and Dox/MnOx-HMCNs against 4T1 and MCF-7/ADR breast cancer cells. The *in vitro* therapeutic efficiency of CPT/MnOx-HMCNs and Dox/MnOx-HMCNs were evaluated by a 3-[4,5-dimethylthiazol-2-yl]-2,5-diphenyltetrazolium bromide (MTT) reduction assay. Typically, 4T1 cells or MCF-7/ADR cells were seeded into a 96-well plate with the cell density of 5×10^3 per well, which were further cultured in 5% CO_2 at 37^{o}C for 24 h. Free CPT and CPT/MnOx-HMCNs (or free Dox and Dox/MnOx-HMCNs) were dispersed into cell culture medium by mild ultrasound treatment, which was further used to substitute the cell culture medium after the cell-seeding process. The equivalent CPT concentrations are 0, 1.25, 2.5, 5, 10, 15, 20 μg/mL, and the equivalent Dox concentrations are 0, 1.25, 2.5, 5, 10, 15, 20, 30 μg/mL. After the co-incubation for 24 h, the culture medium was removed, and the cells were mildly washed with PBS for three times. RPMI 1640 containg MTT (0.6 mg/mL) was added into the cells, which was further cultured for another 4 h. Then, dimethyl sulfoxide (DMSO, 100 μL/well) was added into the plate to replace MTT medium, followed by testing the absorbance by a microplate reader (Bio-TekELx800) at the wavelength of 490 nm. The cell cytotoxicities were calculated as the percentage of cell viabilities of untreated control cells.

***In vitro* hemolysis evaluation.** The *in vitro* hemolysis assay was conducted according to a standard evaluation procedure.[10] Fresh human red blood cells (RBCs) were diluted to 1/10 of initial volume with PBS for the evaluation. Typically, RBCs (0.3 mL) PBS solution was added into different experimental solutions, including PBS (1.2 mL) as the negative control, deionized water (1.2 mL) as the positive control and MnOx-HMCNs (or HMCNs) PBS solution (1.2 mL) with different concentrations ranging from 7.82 – 1000 μg/mL. The mixtures were gently vortexed, followed by standing for 2 h at room

temperature. The RBCs were collected by centrifugation (4000 r/min, 2 min), and the supernatants were obtained for UV-vis test at the wavelength of λ = 541 nm. The hemolysis percentage was calculated using the following equation: Hemolysis% = (A_{sample} – $A_{(-)control}$) / ($A_{(+)control}$ – $A_{(-)control}$). A is the absorbance intensity of UV-vis spectra.

***In vivo* histocompatibility evaluation.** The female nude mice (20 - 25 g) were intravenous injected with MnOx-HMCNs saline solution with different doses (12.5, 25 and 50 mg/kg). The mice received pure saline were used as the control group. The potential toxicity effects were monitored every day. At the end of feeding (15 days and 30 days), the mice were sacrificed and the main organs (heart, liver, spleen, lung and kidney) were taken out and stained with hematoxylin and eosin (H&E) for histopathological analysis. All the animal procedures were performed under the guideline approved by the Institutional Animal Care and Use Committee (IACUC) of the Shanghai Institute of Materia Medica, Chinese Academy of Sciences (CAS).

Characterizations. Transmission electron microscopy (TEM) was carried out on a JEM-2100 electron microscope operated at 200 kV. Scanning electron microscopy (SEM) and element mapping were acquired on a field-emission Magellan 400 microscope (FEI Company). Dynamic light scattering (DLS) was tested on Zetasizer Nanoseries (Nano ZS90). N_2 adsorption-desorption characterization was carried out on a Micrometitics Tristar 3000 system. Confocal laser scanning microscopy (CLSM) images were acquired on FV1000, Olympus, Japan. UV-vis spectra were recorded on a UV-3101PC Shimadzu spectroscope and X-ray photoelectron spectrum was acquired on a ESCAlab250. Raman spectra were recorded on a Thermofisher spectrometer (DXR) with the excitation wavelength of 633 nm. Thermogravimetry (TG) diagrams were obtained on a Netzsch STA 449C microanalyzer in air flow at 10 K/min.

5. Acknowledgement

We acknowledge financial supports from the National Nature Science Foundation of China (Grant No. 51302293), Shanghai Rising-Star Program (14QA1404100), Natural Science Foundation of Shanghai (13ZR1463500), Foundation for Youth Scholar of State Key Laboratory of High Performance Ceramics and Superfine Microstructures (Grant No. SKL201203) and the Science and Technology Support Plan of Zhengjiang City (SH2013080). We acknowledge the experimental supports of Prof. Y. P. Li and Dr. P. F. Xu for the antimetastasis assay and Dr. J. M. Zhang for the hemolysis evaluation.

Notes and references

[a]Department of Radiology, Shanghai Cancer Hospital, Fudan University, Shanghai, 200032, P.R. China. Email: weijunpeng@yahoo.cn

[b]State Key Laboratory of High Performance Ceramics and Superfine Microstructures, Shanghai Institute of Ceramics, Chinese Academy of Sciences, Shanghai, 200050, P. R. China. E-mail: chenyu@mail.sic.ac.cn

[c]Department of Ultrasound, The First People's Hospital of Zhenjiang City, Zhengjiang, 212002, P. R. China.

Dr. S. Zhang and Dr. X. Qian contribute equally to this work.

Electronic Supplementary Information (ESI) available: *In vitro/in vivo* ultrasound imaging, CLSM image and H&E results. See DOI: 10.1039/b000000x/

1. (a) C. D. H. Alarcon, S. Pennadam, C. Alexander, *Chem. Soc. Rev.* 2005, **34**, 276; (b) M. A. C. Stuart, W. T. S. Huck, J. Genzer, M. Muller, C. Ober, M. Stamm, G. B. Sukhorukov, I. Szleifer, V. V. Tsukruk, M. Urban, F. Winnik, S. Zauscher, I. Luzinov, S. Minko, *Nat. Mater.* 2010, **9**, 101; (c) S. Ganta, H. Devalapally, A. Shahiwala, M. Amiji, *J. Control. Release* 2008, **126**, 187; (d) Y. Wang, K. Zhou, G. Huang, C. Hensley, X. Huang, X. Ma, T. Zhao, B. D. Sumer, R. J. DeBerardinis, J. Gao, *Nat. Mater.* 2014, **13**, 204.
2. M. S. Yavuz, Y. Y. Cheng, J. Y. Chen, C. M. Cobley, Q. Zhang, M. Rycenga, J. W. Xie, C. Kim, K. H. Song, A. G. Schwartz, L. H. V. Wang, Y. N. Xia, *Nat. Mater.* 2009, **8**, 935.
3. (a) M. L. Viger, J. Sankaranarayanan, C. D. Lux, M. Chan, A. Almutairi, *J. Am. Chem. Soc.* 2013, **135**, 7847; (b) C. C. Huang, C. Y. Tsai, H. S. Sheu, K. Y. Chuang, C. H. Su, U. S. Jeng, F. Y. Cheng, H. Y. Lei, C. S. Yeh, *ACS Nano* 2011, **5**, 3905.
4. Y. Chen, P. Xu, Z. Shu, M. Wu, L. Wang, S. Zhang, Y. Zheng, H. Chen, J. Wang, Y. Li, J. Shi, *Adv. Funct. Mater.* 2014, **24**, 4386.
5. (a) Y. Chen, H. Chen, J. Shi, *Adv. Mater.* 2013, **25**, 3144; (b) Slowing, II, J. L. Vivero-Escoto, C. W. Wu, V. S. Y. Lin, *Adv. Drug Deliv. Rev.* 2008, **60**, 1278; (c) M. Vallet-Regi, F. Balas, D. Arcos, *Angew. Chem. Int. Ed.* 2007, **46**, 7548; (d) Y. F. Zhu, J. L. Shi, W. H. Shen, X. P. Dong, J. W. Feng, M. L. Ruan, Y. S. Li, *Angew. Chem. Int. Ed.* 2005, **44**, 5083; (e) M. W. Ambrogio, C. R. Thomas, Y. L. Zhao, J. I. Zink, J. F. Stoddartt, *Acc. Chem. Res.* 2011, **44**, 903; (f) J. E. Lee, N. Lee, T. Kim, J. Kim, T. Hyeon, *Acc. Chem. Res.* 2011, **44**, 893; (g) F. Q. Tang, L. L. Li, D. Chen, *Adv. Mater.* 2012, **24**, 1504; (h) P. P. Yang, S. L. Gai, J. Lin, *Chem. Soc. Rev.* 2012, **41**, 3679; (i) Y. Chen, H. R. Chen, J. L. Shi, *J. Inorg. Mater.*, 2013, **28**, 1.
6. (a) C. Chung, Y.-K. Kim, D. Shin, S.-R. Ryoo, B. H. Hong, D.-H. Min, *Acc. Chem. Res.* 2013, **46**, 2211; (b) K. Yang, L. Z. Feng, X. Z. Shi, Z. Liu, *Chem. Soc. Rev.* 2013, **42**, 530.
7. Z. Liu, J. T. Robinson, S. M. Tabakman, K. Yang, H. J. Dai, *Mater. Today* 2011, **14**, 316.
8. L. Cao, X. Wang, M. J. Meziani, F. S. Lu, H. F. Wang, P. J. G. Luo, Y. Lin, B. A. Harruff, L. M. Veca, D. Murray, S. Y. Xie, Y. P. Sun, *J. Am. Chem. Soc.* 2007, **129**, 11318.
9. (a) Y. Chen, P. Xu, M. Wu, Q. Meng, H. Chen, Z. Shu, J. Wang, L. Zhang, Y. Li, J. Shi, *Adv. Mater.* 2014, **26**, 4294; (b) T. W. Kim, P. W. Chung, Slowing, II, M. Tsunoda, E. S. Yeung, V. S. Y. Lin, *Nano Lett.* 2008, **8**, 3724; (c) Y. Fang, D. Gu, Y. Zou, Z. X. Wu, F. Y. Li, R. C. Che, Y. H. Deng, B. Tu, D. Y. Zhao, *Angew. Chem. Int. Ed.* 2010, **49**, 7987.
10. Y. Chen, P. Xu, H. Chen, Y. Li, W. Bu, Z. Shu, Y. Li, J. Zhang, L. Zhang, L. Pan, X. Cui, Z. Hua, J. Wang, L. Zhang, J. Shi, *Adv. Mater.* 2013, **25**, 3100.
11. X. P. Dong, W. H. Shen, J. L. Gu, L. M. Xiong, Y. F. Zhu, Z. Li, J. L. Shi, *J. Phys. Chem. B* 2006, **110**, 6015.
12. (a) T. Kim, E. J. Cho, Y. Chae, M. Kim, A. Oh, J. Jin, E. S. Lee, H. Baik, S. Haam, J. S. Suh, Y. M. Huh, K. Lee, *Angew. Chem. Int. Ed.* 2011, **50**, 10589; (b) T. Kim, E. Momin, J. Choi, K. Yuan, H. Zaidi, J. Kim, M. Park, N. Lee, M. T. McMahon, A. Quinones-Hinojosa, J. W. M. Bulte, T. Hyeon, A. A. Gilad, *J. Am. Chem. Soc.* 2011, **133**, 2955; (c) K. M. L. Taylor, J. S. Kim, W. J. Rieter, H. An, W. L. Lin, W. B. Lin, *J. Am. Chem. Soc.* 2008, **130**, 2154.
13. Z. Liu, X. M. Sun, N. Nakayama-Ratchford, H. J. Dai, *ACS Nano* 2007, **1**, 50.
14. F. Buciuman, F. Patcas, R. Craciun, D. R. T. Zahn, *Phys. Chem. Chem. Phys.* 1999, **1**, 185.
15. Z. Shu, Y. Chen, W. M. Huang, X. Z. Cui, L. X. Zhang, H. R. Chen, G. B. Zhang, X. Q. Fan, Y. X. Wang, G. J. Tao, D. N. He, J. L. Shi, *Appl. Catal. B-Environ.* 2013, **140**, 42.
16. (a) M. F. Bennewitz, T. L. Lobo, M. K. Nkansah, G. Ulas, G. W. Brudvig, E. M. Shapiro, *ACS Nano* 2011, **5**, 3438; (b)Y. Chen, D. Ye, M. Wu, H. Chen, L. Zhang, J. Shi and L. Wang, *Adv. Mater.*, 2014, **26**, 7019; (c) Z. Zhao, H. Fan, G. Zhou, H. Bai, H. Liang, R. Wang, X. Zhang and W. Tan, *J. Am. Chem. Soc.*, 2014, **136**, 11220; (d) K. Dong, Z. Liu, J. Liu, S. Huang, Z. Li, Q. Yuan, J. Ren and X. Qu, *Nanoscale*, 2014, **6**, 2211.
17. Y. Chen, Q. Yin, X. F. Ji, S. J. Zhang, H. R. Chen, Y. Y. Zheng, Y. Sun, H. Y. Qu, Z. Wang, Y. P. Li, X. Wang, K. Zhang, L. L. Zhang, J. L. Shi, *Biomaterials* 2012, **33**, 7126.
18. H. B. Na, J. H. Lee, K. J. An, Y. I. Park, M. Park, I. S. Lee, D. H. Nam, S. T. Kim, S. H. Kim, S. W. Kim, K. H. Lim, K. S. Kim, S. O. Kim, T. Hyeon, *Angew. Chem. Int. Ed.* 2007, **46**, 5397.
19. H. Yang, Y. M. Zhuang, H. Hu, X. X. Du, C. X. Zhang, X. Y. Shi, H. X. Wu, S. P. Yang, *Adv. Funct. Mater.* 2010, **20**, 1733.

20. J. Huang, J. Xie, K. Chen, L. H. Bu, S. Lee, Z. Cheng, X. G. Li, X. Y. Chen, *Chem. Commun.* 2010, **46**, 6684.
21. Y. Chen, H. Chen, S. Zhang, F. Chen, S. Sun, Q. He, M. Ma, X. Wang, H. Wu, L. Zhang, L. Zhang, J. Shi, *Biomaterials* 2012, **33**, 2388.
22. H. S. Choi, W. Liu, P. Misra, E. Tanaka, J. P. Zimmer, B. I. Ipe, M. G. Bawendi, J. V. Frangioni, *Nat. Biotechnol.* 2007, **25**, 1165.
23. Z. Liu, A. C. Fan, K. Rakhra, S. Sherlock, A. Goodwin, X. Y. Chen, Q. W. Yang, D. W. Felsher, H. J. Dai, *Angew. Chem. Int. Ed.* 2009, **48**, 7668.
24. (a) Y. Chen, H. R. Chen, L. M. Guo, Q. J. He, F. Chen, J. Zhou, J. W. Feng, J. L. Shi, *ACS Nano* 2010, **4**, 529; (b) Y. Chen, H. R. Chen, D. P. Zeng, Y. B. Tian, F. Chen, J. W. Feng, J. L. Shi, *ACS Nano* 2010, **4**, 6001; (c) Y. Chen, H. R. Chen, J. L. Shi, *Acc. Chem. Res.* 2014, **47**, 125.
25. H. J. Kim, H. Matsuda, H. S. Zhou, I. Honma, *Adv. Mater.* 2006, **18**, 3083.
26. P. Xu, Q. Yin, J. Shen, L. Chen, H. Yu, Z. Zhang, Y. Li, *Int. J. Pharm.* 2013, **454**, 21.
27. J. M. Rosenholm, E. Peuhu, J. E. Eriksson, C. Sahlgren, M. Linden, *Nano Lett.* 2009, **9**, 3308.
28. J. Lu, M. Liong, J. I. Zink, F. Tamanoi, *Small* 2007, **3**, 1341.
29. J. H. Liu, Y. X. Zhao, Q. Q. Guo, Z. Wang, H. Y. Wang, Y. X. Yang, Y. Z. Huang, *Biomaterials* 2012, **33**, 6155.
30. (a) Y. Gao, Y. Chen, X. F. Ji, X. Y. He, Q. Yin, Z. W. Zhang, J. L. Shi, Y. P. Li, *ACS Nano* 2011, **5**, 9788; (b) Y. Chen, H. Chen, J. Shi, *Mol. Pharm.* 2014, **11**, 2495.
31. (a) Y. S. Lin, C. L. Haynes, *J. Am. Chem. Soc.* 2010, **132**, 4834; (b) Slowing, II, C. W. Wu, J. L. Vivero-Escoto, V. S. Y. Lin, *Small* 2009, **5**, 57.
32. C. Urata, H. Yamada, R. Wakabayashi, Y. Aoyama, S. Hirosawa, S. Arai, S. Takeoka, Y. Yamauchi, K. Kuroda, *J. Am. Chem. Soc.* 2011, **133**, 8102.

